Accepted Manuscript

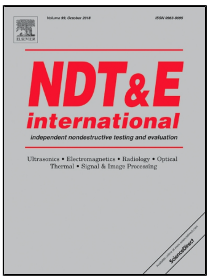

Improving elevation resolution in phased-array inspections for NDT

J. Brizuela, J. Camacho, G. Cosarinsky, J.M. Iriarte, J.F. Cruza

PII:	S0963-8695(18)30155-5
DOI:	10.1016/j.ndteint.2018.09.002
Reference:	JNDT 2020
To appear in:	*NDT and E International*
Received Date:	09 March 2018
Accepted Date:	03 September 2018

Please cite this article as: J. Brizuela, J. Camacho, G. Cosarinsky, J.M. Iriarte, J.F. Cruza, Improving elevation resolution in phased-array inspections for NDT, *NDT and E International* (2018), doi: 10.1016/j.ndteint.2018.09.002

Improving elevation resolution in phased-array inspections for NDT

J. Brizuela[1], J. Camacho[2*], G. Cosarinsky[3], J.M. Iriarte[3], J. F. Cruza[2].

[1] National Scientific and Technical Research Council (CONICET), Buenos Aires, Argentina
J. Brizuela: josebrizuela@conicet.gov.ar (corresponding author);

[2] Spanish National Research Council (CSIC), Madrid, Spain
J. Camacho: j.camacho@csic.es
J. F. Cruza: jorge.f.cruza@csic.es

[3] National Atomic Energy Commission (CNEA), Buenos Aires, Argentina
G. Cosarinsky: cosarinsky@cnea.gov.ar
J. M. Iriarte: iriarte@cnea.gov.ar

*Author to whom correspondence should be addressed to j.camacho@csic.es

Abstract

The Phased Array Ultrasonic Technique (PAUT) offers great advantages over the conventional ultrasound technique (UT), particularly because of beam focusing, beam steering and electronic scanning capabilities. However, the 2D images obtained have usually low resolution in the direction perpendicular to the array elements, which limits the inspection quality of large components by mechanical scanning. This paper describes a novel approach to improve image quality in these situations, by combining three ultrasonic techniques: Phased Array with dynamic depth focusing in reception, Synthetic Aperture Focusing Technique (SAFT) and Phase Coherence Imaging (PCI). To be applied with conventional NDT arrays (1D and non-focused in elevation) a special mask to produce a wide beam in the movement direction was designed and analyzed by simulation and experimentally. Then, the imaging algorithm is presented and validated by the inspection of test samples. The obtained images quality is comparable to that obtained with an equivalent matrix array, but using conventional NDT arrays and equipments, and implemented in real time.

Keywords

Phased array resolution; industrial NDT; synthetic aperture imaging; phase coherence imaging; 3D imaging.

I. Introduction

The Phased Array Ultrasonic Technique (PAUT) has become a popular technique in many NDT fields. Frequently, PAUT uses linear phased arrays to produce 2D-images of the azimuth plane. Here, the identification of defects is often limited by their random orientation or by the operator's experience [1]. One approach to increase the probability of detection is to extend the angular range and orientation of the scan. Even better, it would be desirable to have a complete 3D representation of the inspected volume of interest (VOI) to more easily identify and evaluate defects.

Even though 3D ultrasonic imaging is a widespread and a highly-developed modality in the medical field, it is rarely applied in NDT. The main challenges for an industrial 3D imaging system are to have many channels to handle the large number of elements of a matrix transducer and to be able of acquiring, processing and transfer large amounts of data in real time when scanning a full volume. Usually, 25 frames per second (fps) are required for real-time visualization in the medical field, but the automatic inspection of large industrial components could require a higher figure.

The simplest way for scanning a 3D volume is to acquire thin slices of the VOI with a linear array to get a series of 2D-images. Typically, a motorized mechanical support integrated within the transducer housing is used to move, tilt or rotate the linear array, which yields to different geometries of the acquired VOI [2]. However, the transducer-scanner embedded arrangement is only able to insonify a limited VOI from a fixed position. Other approaches are supported by external mechanisms that track the array position with high accuracy [3]. Methods known as *freehand 3D ultrasound scanning* have positioning systems based on electromagnetic [4] or optical sensors [5], which are attached to the probe and allow moving the transducer freely. In this case, images are acquired with their relative position and orientation, so it is possible to reconstruct a large volume. Nonetheless, these alternatives require a calibration process after the acquisition to establish size and limits of the scanned VOI and the data scaling [6].

The linear array allows performing an electronic scan in the azimuth or *xz* plane, where *x* and *z* are the array element and propagation directions, respectively. The ultrasonic beam can be focused in reception using dynamic focusing techniques, enhancing the lateral resolution at all depths. Nevertheless, in elevation (*y*-direction) the linear array aperture is passive, and the lateral resolution cannot be electronically improved. Therefore, some strategy should be used to reduce the slice thickness in the elevation direction to improve resolution.

Focused acoustic lenses are usually incorporated to reduce the beam profile in the elevation plane [7]. This solution is delivered by the arrays manufacturer, who includes the lens in the transducer impedance matching layer. However, the mechanical lens determines an elevation focal distance that provides good resolution in the *y*-direction within its focal length only. On the other hand, the slice thickness of linear arrays can be reduced by splitting the elements in the elevation direction. 1.25D arrays offer rows elements that are symmetrically connected around the centre elevation element and no additional beamforming channels are required. The 2D image thickness is reduced in the elevation plane but focusing remains limited. In the case of 1.5D arrays, row elements can be individually controlled, but symmetric about the *y*-direction centreline. Thus, elevation aperture and focusing can be dynamically variable. In the 1.75D array, row elements have no symmetry constraint and allow some steering in the elevation plane [8, 9]. Another alternative is the 2D array, which allows scanning a solid angle with a narrow beam. Two-dimensional beam steering can be also accomplished with dynamic focusing techniques, which provide significant improvements in 3D-images quality [10]. However, 1.75D or 2D arrays require increased hardware complexity to control large apertures [11, 12]. Several developments have been carried out to reduce the number of channels required to control full half-wavelength apertures and achieve high-frame rates. For example, larger apertures have been synthetized using sparse arrays, which consists in relocating or multiplexing smaller apertures, trying to approach the original two-way fully populated radiation pattern [13]. Another approach consists on an arrangement of multiple 1D-arrays for synthesizing a 2D-virtual array, which allow high speed of electronic scanning and lateral resolution improvement [14].

For 3D imaging, the VOI reconstruction is performed using the set of 2D images acquired at regular intervals as data source, but the volume must be displayed in a 3D integer grid of volumetric pixels (*voxels*). In general, the reconstruction involves three basic steps: *resampling* the 2D-image into the VOI for determining the voxels values; *interpolating* the contribution of the projected slice to those close voxels; and *rendering* the resultant volume [5]. Rendering techniques allow visualizing the data volume as a 3D image. The most usual methods are: *Multi-Planar Rendering*, which re-slices the structure according to different directions of the 2D-images and does not require too many calculations [15]. *Surface rendering*, which show the 3D volume as a set of tangible surfaces that can be extracted and visualized (isosurfaces) [16]. *Volume Rendering* uses properties such as opacity, colour, scattering and emissivity to plot the volume.

While in the medical field the transducer is in contact with the tissue and only one propagation medium is considered, a more complex scenario must be addressed in industry. In fact, imaging must be performed on a layered structure of materials, usually with different propagation velocities. Thus, to obtain a 2D-image, refraction of the ultrasound waves at the interfaces complicates the calculation of the propagation delays necessary for beamforming. Moreover, computing delays is more difficult when interface shape is unknown, like in large tolerance manufacturing processes or when inspecting large components of

complex shape. These major challenges have limited the use of 3D imaging for NDT in industry. However, some industrial applications have been successfully developed [17, 18].

This work proposes, for industrial NDT applications, an alternative method to generate 3D ultrasonic images that allows VOI reconstruction taking advantage of three image modes: Phased Array, Synthetic Aperture Focusing and Phase Coherence Imaging. A conventional linear array is used to collect data in pulse-echo linear B-Scan mode with dynamic depth focusing, reducing the data volume and improving SNR with regard to single-element methods like Full Matrix Capture (FMC). However, the array probe is mounted with a specifically designed mask for achieving an unfocused elevation beam (divergent). Therefore, there is no need for introducing hardware changes or major investments in specific arrays during the inspection set-up stage, given that the mask can be constructed at relative low cost and the beam width can be modified for inspecting different types of materials. For the final implementation, an array with reduced element length could be used if the mask limits the method applicability in some way.

Even though the lateral resolution of each 2D-image in the elevation direction becomes poor because of the mask effect, these low-resolution images are combined in a coherent way by SAFT by software post-processing, which significantly improves the elevation resolution and the SNR. Then, the PCI technique is employed for reducing side lobes and grating lobes in the final image, overcoming the usual limitation of SAFT. Furthermore, all the process is performed by assuming two media with different propagation velocity, the common situation in NDT. The image processing is performed exploiting the computing power of GPU, which allows the VOI reconstruction at high-speed.

The objective of this work is to provide a high-resolution 3D imaging method to be implemented with conventional phased-array probes and equipments, instead of usually expensive matrix arrays with associated large parallel channel count electronics, thus reducing the cost of this kind of inspections. Furthermore, as most of the beamforming process is carried out in real-time by the phased-array hardware, inspection time, data volume and post-processing complexity are reduced with regard to single-element acquisition schemes like FMC, which is an additional advantage.

The broad beam generation strategy for both contact and immersion conditions is described and supported by simulations and experiments in the next section. Section III explains the image reconstruction algorithm using SAFT and PCI. On Section IV, experimental validation is carried out on different test-blocks and in a nuclear plant coupon. Finally, on Section V, conclusions and forward-looking statements are given.

II. Defocusing masks design and validation

Conventional linear arrays have a single line of elements, which allows beam focusing and steering only in the azimuth plane. Regardless of the scan mode that might be use, the axial resolution is determined by the fundamental frequency and bandwidth of the transducers elements, while the lateral resolution is related to the frequency and size of the active aperture. Thus, the 2D-image resolution requirements can be achieved with the proper selection of the array construction parameters and active aperture size.

On the other hand, linear arrays do not provide control capabilities on the elevation-axis. Their design usually includes a relatively large passive-aperture to guarantee signal strength and sensitivity, which yields to produce a collimated beam with poor lateral resolution on the elevation plane. In general, the passive aperture of the elements (W) has a value $W \geq 10\lambda$ (where λ means the wavelength value corresponding to the centre frequency of the array), and hence, the 2D image does not represent a thin section of the VOI (Figure 1A). According to Full Width at Half Maximum (FWHM) criterion [19], the beam spread half-angle (α_y) for the passive-aperture W measured at 6dB drop is:

$$\alpha_y = \sin^{-1}\left(0.5\frac{\lambda}{W}\right) \tag{1}$$

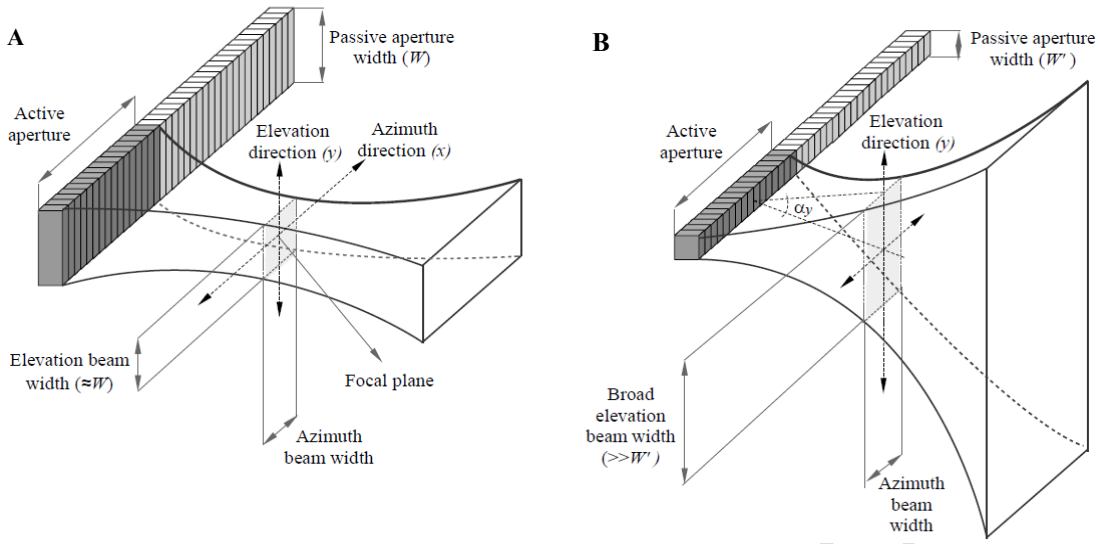

Figure 1. A) – Beam profile for a conventional linear array. The lateral resolution in the elevation plane is similar to the passive aperture width (≈*W*). **B) -** Beam profile for a linear array with a small passive aperture (*W'*). The lateral resolution in the elevation plane is worse than *W*.

Therefore, the smaller the *W* parameter, the wider the beam spread (α_y) (Figure 1B). The approach followed in this work is to reduce the passive aperture of a conventional linear array to values as low as one wavelength for obtaining a broad enough beam for synthetic imaging in the *y* direction. The corresponding decrease in SNR, will be partially compensated by the averaging effect of the SAFT in the array movement direction.

Two alternatives were evaluated by simulation and experimentally for the most common NDT industrial applications: water immersion and contact by gel coupling. The different arrangements array-mask were simulated considering a linear array of 5 MHz, 32 elements, 60% of bandwidth, pitch of 0.5 mm (gap of separation between elements 0.1 mm), and 10 mm of passive aperture.

A. Mask for immersion inspections

A V-shaped silicone mask was designed to produce a divergent elevation-beam from a conventional linear array. Silicone is a low-cost material that can be easily shaped, and it is stable for a long time. Unlike the sound propagation in water with $c_{H2O} \approx 1.48$ mm.us^{-1} and low attenuation coefficient, the silicone rubber has a lower velocity ($c_S \approx 1.03$ mm.us^{-1}) and higher acoustical attenuation (14.0 dB.cm^{-1}) [20]. These features lead to emulate a narrow-phased array probe by leaving a thin window without silicone on the sensor surface and avoid expending in a new one.

The ultrasonic beam pattern will spread out from the small opening of size W_S in the centre of the mask (Figure 2). Thus, for an opening of $W_S = 1.5$ mm mounted on a 5 MHz linear array immersed in water ($\lambda \approx 0.3$ mm), the half-angle that defines the main-lobe width according to (1) is $\alpha_{y(H2O)} \approx 6°$. To avoid the sound propagating through the mask and then to the water, generating unwanted signals and besides using a highly attenuating material, the mask walls angle is calculated to provide total reflection inside the silicone, by following Snell's law:

$$\theta \geq \sin^{-1}\left(\frac{c_S}{c_{H_2O}}\right) = 44° \qquad (2)$$

.

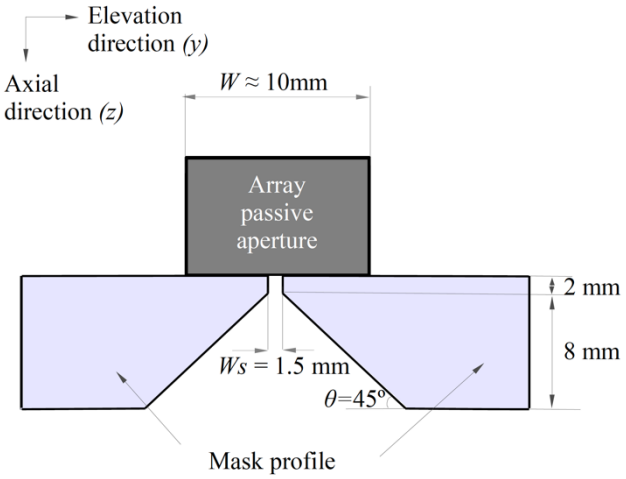

Figure 2. Silicone mask design use to reduce the array elements passive aperture in the elevation plane.

The performance of an array mounted in contact with a silicone mask, which includes a 1.5 mm slot, was analysed in two scenarios: all the set immersed in water to simulate the propagated beam and, then, including an aluminium block as a test piece to assess the acoustic beam inside the component. Simulations were carried out with CIVA 2016 (Extende, France) [21].

First, computing was performed within a VOI of 10x30x40 mm located 14.5 mm from the surface of the array (directions of azimuth, elevation, and depth, are represented in simulations as coordinates *x*, *y*, *z*, respectively). A single focal law was configured using 32 elements of active aperture, focusing at 40 mm from the surface of the array. All simulation results are referenced to the VOI position (Figure 3A and 3B). On the azimuth focal plane, the maximum acoustic amplitude is located at $z = 24.5$ mm (Figure 3C) from the reference position (14.5 mm). On the elevation plane, the mask behaves as expected, broadening the beam in the elevation direction (Figure 3D). According to the simulation values, the beam width in the elevation plane at the focus depth is 8.5 mm measured at -6 dB. Therefore, the half-angle of divergence in water at 40 mm is $\alpha_{y(H_2O)} = \tan^{-1}(4.25/40) \approx 6°$, as expected.

In another simulation, an aluminium block 35 mm thick was located at 28 mm distance from the array surface. The array-mask configuration was not modified from the previous case. However, the focal law was changed to focus at 12 mm within the material in the azimuth plane, so the focal point distance remains at 40 mm from the array surface (Figure 4A). Considering the signal level of the computed beam in water as a reference (0 dB), it is necessary to increase the gain to compensate for signal loss in the aluminium block (note that in the colour scale of Figure 4B and 4C an additional gain of 6 dB have been introduced). According to the simulation, the lateral resolution on the azimuth focal plane is 1.7 mm, measured at 6 dB drop. On the elevation plane, the beam profile opens even more because of refraction at the interface (Figure 4C). So, the elevation beam width results in 15.6 mm for a 6 dB drop, the half-angle of divergence is $\alpha_{y(Al)} = \tan^{-1}(0.5 \cdot 15.6/12) \approx 26.2º$.

Finally, the focal point spot on the axial plane (*xy* plane) is compared for the two cases analysed. The focal spot in water has 1.2x8.5 mm (*xy* dimensions, determined for a 6 dB drop), whereas in aluminium it has 1.7x15.6 mm (azimuth and elevation, respectively). Therefore, for the same array-mask arrangement, the focus lateral width in the elevation direction in the aluminium increases by 84% with respect to that in water (Figure 5), which provides an even wider beam for applying SAFT inside the component.

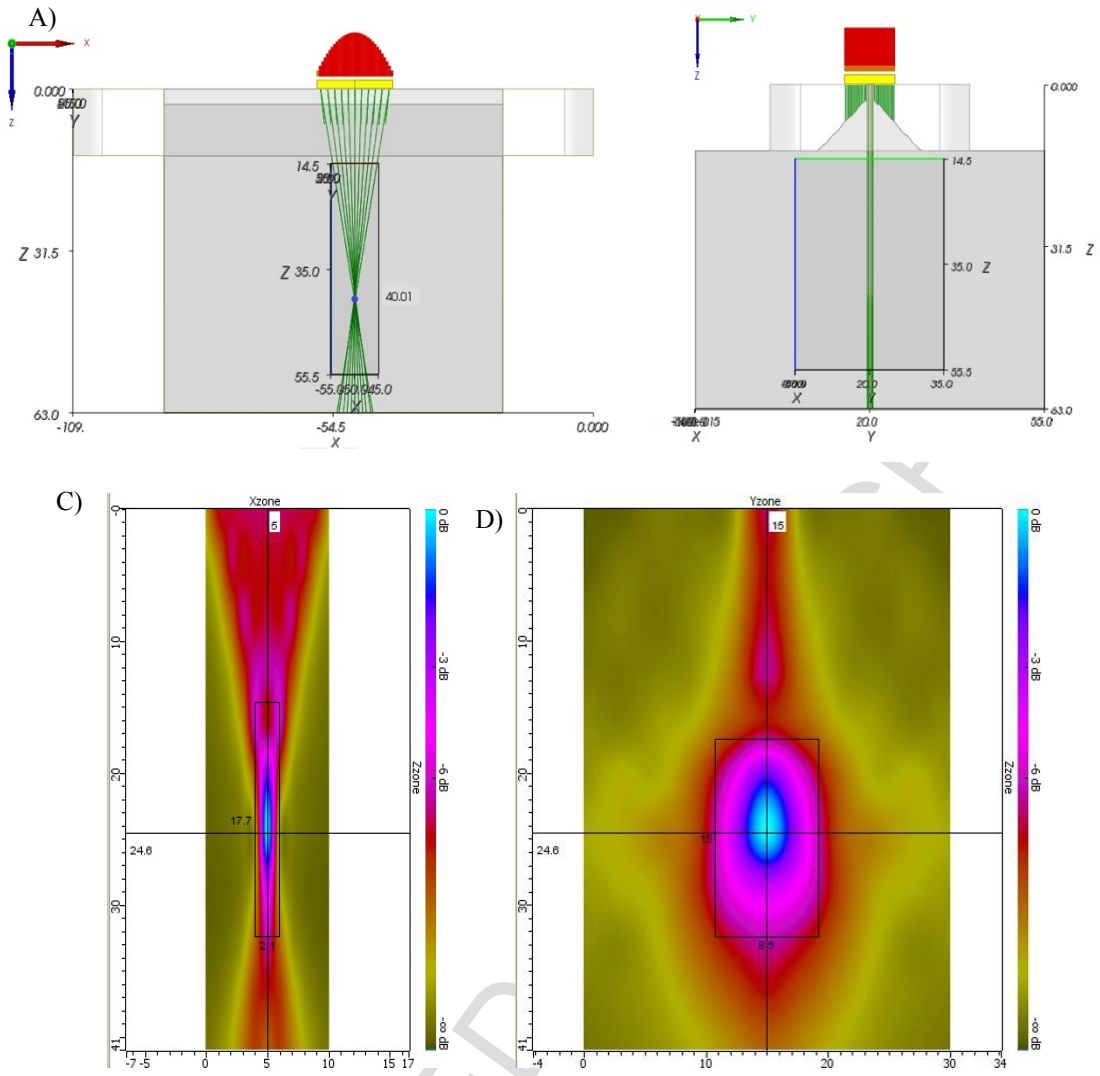

Figure 3. Simulation results with a silicone mask in water (dimensions in mm). **A) –** Azimuth plane view of the configured scenario with the focal laws represented above the array for a focus at 40 mm depth. **B) –** Elevation plane view of the silicone mask used for reducing the passive aperture. **C)-** Field in the azimuth focal plane. **D)-** Field in the elevation plane; observe the broad beam generated.

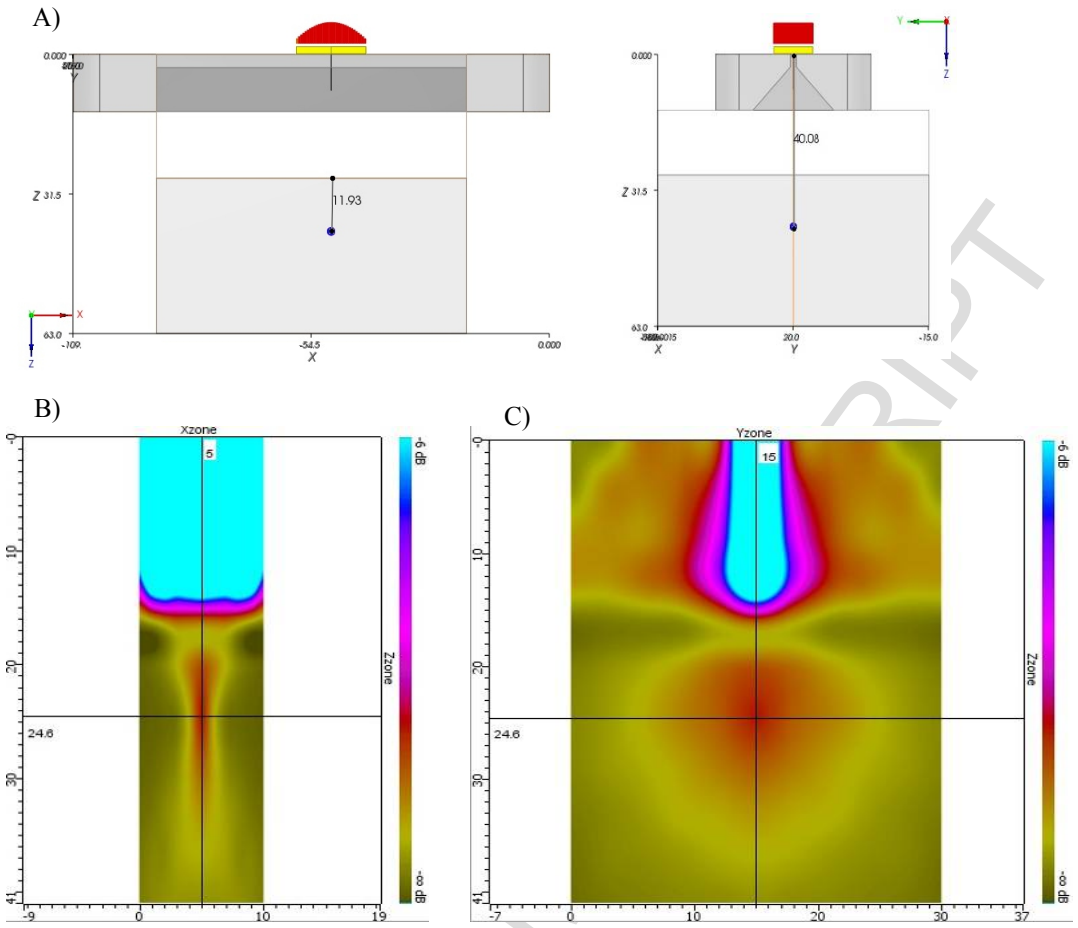

Figure 4. Simulation of a silicone mask in water and within an aluminium block. A 6 dB extra gain was used for field visualization in the aluminium. **A) –** Simulated scenario (left: azimuth view; right: elevation view). The beam focus is placed at 40 mm depth (15 mm inside the block). **B) –** Field in the azimuth focal plane. **C)-** Elevation beam profile, observe that beam refracted in aluminium is even wider than in water.

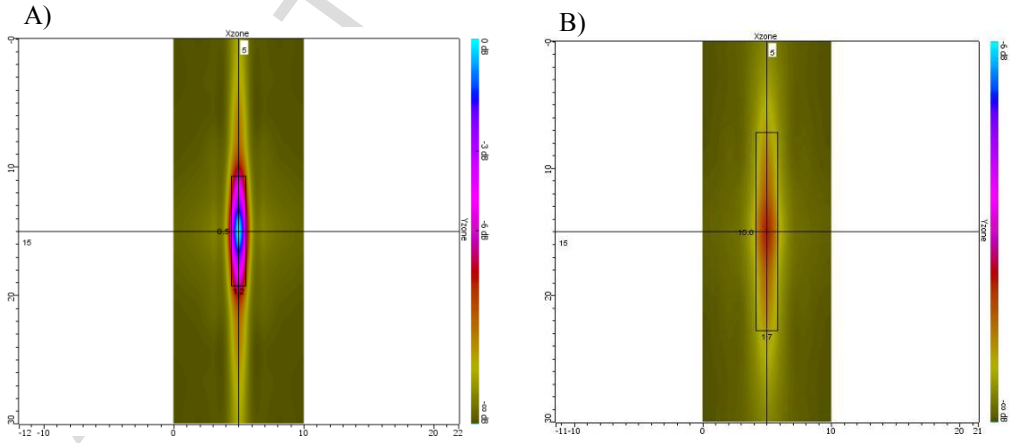

FFigure 5. Comparison between the focal planes for the same axial distance of the array (units in mm). **A) –** Focal spot in water. **B) –** Focal spot in aluminium.

B. Mask design for contact inspections

A trapezoidal-shape mask was designed for operating in direct contact with flat surfaces. Its topside, in contact with the array, determines the active area of the elements in the elevation direction. A mask mechanized in Rexolite® ($c_R \approx 2.32$ mm.us^{-1}), of height $H = 22$ mm and a contact surface $W_R = 1$ mm was considered for the simulation (Figure 6). According to (1), the expected beam divergence inside the mask material for a 5 MHz array and $W_R = 1$ mm, with $\lambda \approx 0.46$ mm is $\alpha_{y(Rex)} \approx 14$ °. Again, the side wall mask angle was set above the critical angle: $\theta = \sin^{-1}(c_{H2O}/c_R) \geq 40°$, to avoid sound travelling through the gel coupling to propagate into the mask.

The simulation was performed in pulse-echo with a flat bottom hole (FBH) 1 mm diameter at 15 mm depth in an aluminium block of thickness $T = 30$ mm. The array and the mask were virtually moved over the block surface over a length of 60 mm in the elevation direction (y-axis) and the reflector response was evaluated every 5 mm (Figure 6A).

The effect of reducing the passive aperture of the array elements by the wedge and scanning over the reference reflector can be observed in Figure 6B. The divergent beam in the elevation direction causes the reflector tip to be detected from different positions, describing a hyperbola centred on the FBH. From this result, the beam divergence on the elevation direction is nearly 40º, considering a 6 dB drop. This value matches with the refracted angle at the interface at $\alpha_{y(Rex)}$ as can be verified by Snell's law.

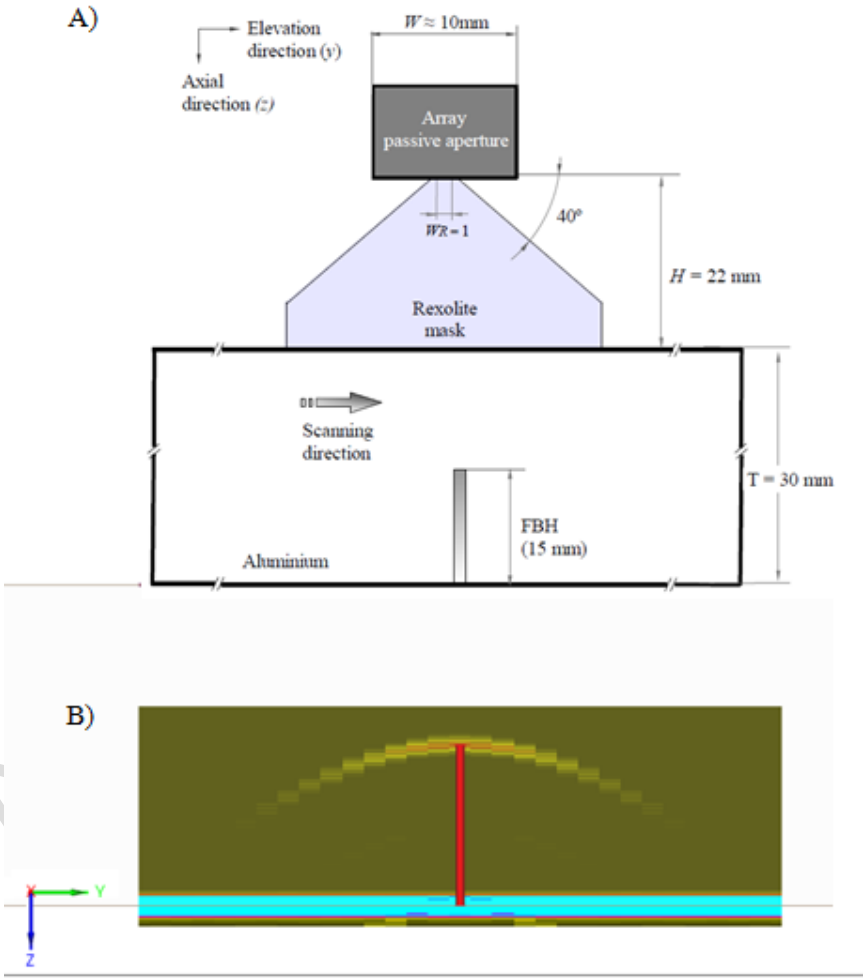

Figure 6. A)- Simulated scheme based on the trapezoidal wedge design. **B)-** Hyperbola produced by the scattered echo from the FBH tip during the scanning along y axis.

III. Image reconstruction

By widening the beam in the y direction by the use of a mask, several B-Scan images acquired in pulse-echo and linear electronic scanning with dynamic focusing can be combined in that direction by SAFT. Different from Full Matrix Capture (FMC), this strategy allows collecting focused images in the azimuthal plane, with better signal-to-noise ratio because of focused emission (linear scan instead of single-element acquisition) and reduced data volume because of hardware beamforming, leaving the processing for the elevation direction only. If enough B-Scan images are used at a given voxel, the resultant resolution in the *y* direction can be improved with regard to using a conventional array with a large elevation aperture. Furthermore, as the samples at all depths are focused with SAFT, the result will be better than using an array with an elevation focus at a single depth. Between all the variants and strategies on SAFT, the *monostatic* method was used for achieving a spatial and coherent composition on the elevation direction [22, 23, 24]. This approach also offers a fast-numerical reconstruction.

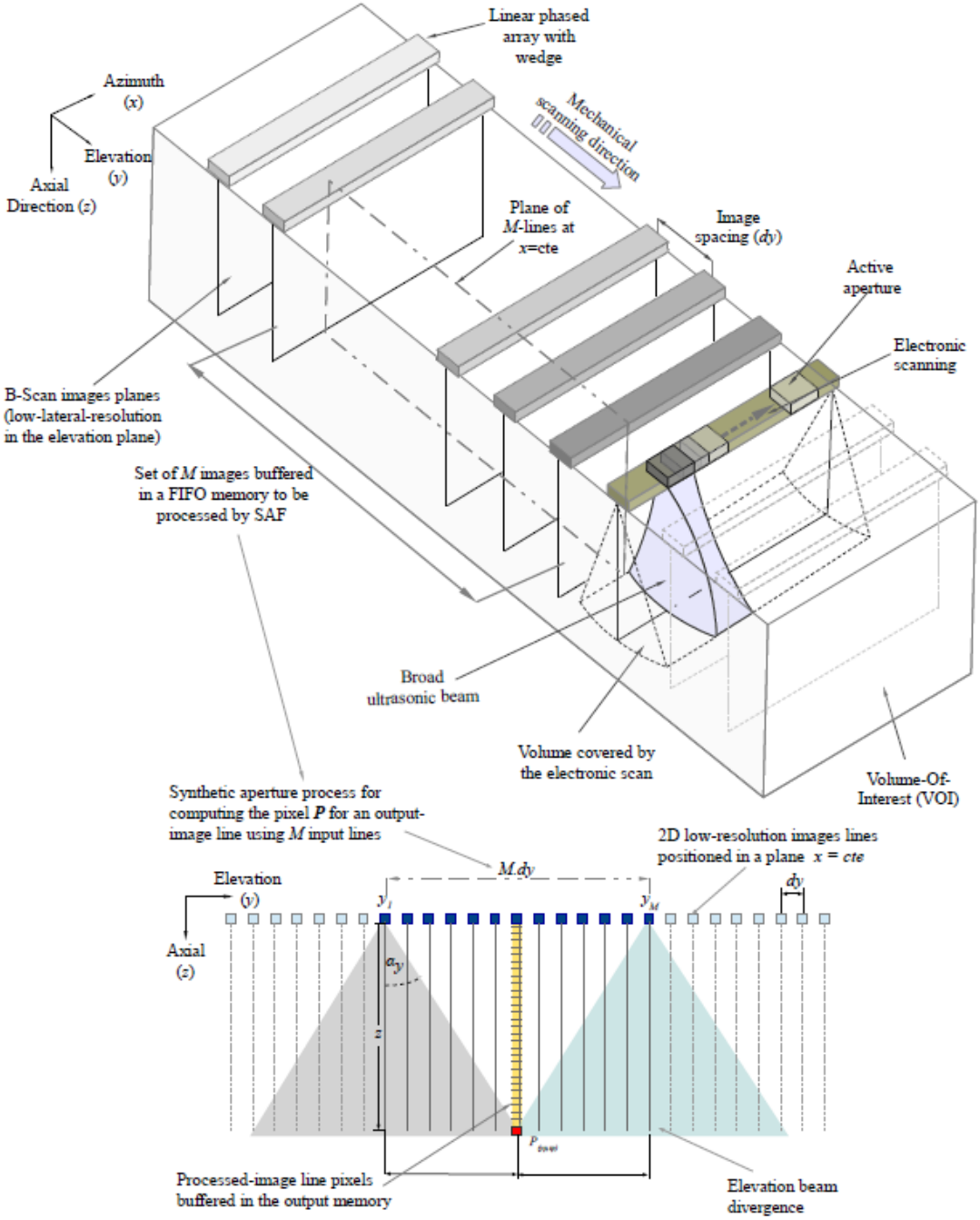

Figure 7. Scheme for the VOI scanning (above) and imaging processing for an output image line (below).

The VOI is sampled at spatial intervals between each 2D images no greater than λ/2 to limit the formation of grating lobes [25]. The 2D images can be acquired on B or S scans formats using pulse-echo mode and dynamic focusing on the azimuth plane.

Each image is formed by *L* lines (A-Scans) and visualizes a cross-sectional image through a vertical slice of the VOI. However, the broad beam on the elevation plane introduces on the 2D-image scattering information that belongs to adjacent regions. After buffering in a FIFO[1] memory a set of *M* low-resolution images, the monostatic SAFT is applied for composing a thinner slice of the VOI. As a result, a higher resolution image is obtained that is spatially located in the centre of the selected *M*-images, and it is stored in an output buffer (Figure 7).

The output image is reconstructed line-by-line, extracting the information from the A-scans that belongs to the same elevation plane. Each pixel of the output line (focus point) is obtained from a set of *M*-samples that are chosen by considering the round-trip TOF from each focus to each input line position. Thus, each selected sample corresponds to the same spatial point to compose. Once all lines of the output image are completed, a new low-resolution image is inserted into the input buffer memory and the older input is discarded. This process is repeated for each image that is acquired and allows gradually forming the explored VOI.

The SAFT composition process enhances the SNR in the output image, since each pixel represents the average of *M*-samples and the incoherent noise is reduced by $\sqrt{M}$. Furthermore, the composition process is equivalent to operate with an array of *M* elements in the elevation direction. The achieved lateral resolution Δy is given by the Rayleigh criterion which defines the main-lobe width between zeros in the elevation plane measured at a depth z [26]:

$$\Delta y = z.\sin^{-1}\left(\frac{\lambda}{M.dy}\right) \tag{3}$$

where *dy* is the mechanical scan step in the elevation direction and *z* is depth. Thus, for an array of 5 MHz, operating in contact with aluminium ($c_{Al} \approx 6.2$ mm.us^{-1}), with $dy = \lambda/2$, and $M = 10$, the lateral resolution in the elevation plane at $z = 15$ mm will be $\Delta y \approx 3$ mm. This value is better than that provided by a conventional linear array non-focused in elevation, which generates a typical beam width between 10 and 20 mm at the same depth.

According to (3), the elevation lateral resolution improves for higher *M* values. However, the practical limit of Δy is given by the beam divergence in the elevation plane (α_y) and limited by the wavelength (λ). In other words, the output pixel must be contained by all the beams to be processed (Figure 7). Thus, the number of consecutive images (M_{max}) spaced at *dy* required to compute the pixel *P*, which is located at the axial distance *z*, is given by:

$$M_{\max} = \left|\frac{2z}{dy}\tan(\alpha_y)\right|_{\downarrow} \tag{4}$$

where the operator $|\cdot|_{\downarrow}$ expresses rounding downwards. Thus, according to (4), the maximum number of images to be composed depends on the axial distance, which means that a *dynamic aperture* process should be used. That is, as the sound progresses in the material, more images can be included to achieve the best possible resolution at all depths.

The amplitude of each output pixel is obtained from the sum of the *M*-input samples. The simplest case is for a homogeneous medium with a speed of propagation c_1 (Figure 8A), in which the round-trip TOF from an array position y_i to a pixel *P* of coordinates (y_P, z_P) in the elevation plane is:

$$t_{Pi} = \frac{2}{c_1}\left|\vec{r}_{iP}\right| = \frac{2}{c_1}\sqrt{\left(y_i - y_P\right)^2 + {z_P}^2} \tag{5}$$

[1] First -In First-Out Memory.

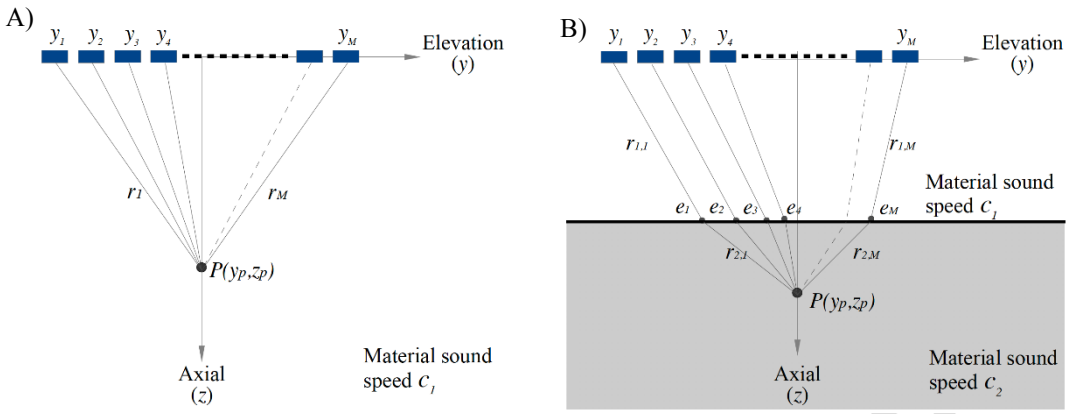

Figure 8. Geometric considerations to calculate the amplitude at each pixel according to the application scenario **A)-** a single medium. **B)-** Two media with a flat-interface.

where $i = \{1, \ldots, M\}$ is the acquisition order, and $\vec{r}_{iP}$ means the distance from the array elevation position y_i to the pixel P. Afterwards, the index idx of the A-scan sample corresponding to the pixel P for the position i is obtained as a function of the TOF as:

$$idx_{Pi} = \left| f_S . t_{Pi} \right|_{\updownarrow} \tag{6}$$

where f_S is the sampling frequency and the operator $|\cdot|_{\updownarrow}$ expresses rounding. The intensity of each output pixel (I_P) is obtained from M delayed samples by:

$$I_P = \frac{1}{M}\left|\sum_{i=1}^{M} A_i(idx_{Pi})\right| \tag{7}$$

where $A_i(n)$ is the analytical representation of the A-Scan signal received by the array at the position y_i, obtained from a real A-Scan $a_i(n)$ of n-samples after applying the Hilbert transform $H(\cdot)$:

$$A_i(n) = a_i(n) + jH\left(a_i(n)\right) \tag{8}$$

The absolute value in (7) is for the envelope extraction of the signal, which allows visualizing the ultrasound output image in video format. Furthermore, the formation process indicated by (7) must be repeated for the L-lines that are contained in each input image.

The SAFT process is more complex when an interface between two materials is included (Figure 8B). The sound emitted from a position y_i reaches the materials boundary at the entry point e_i and is refracted before continuing to the pixel P. According to the Fermat's principle the sound will follow the path with the minimum travel time. Thus, the interface should be finely discretized to achieve an acceptable resolution in the TOF, and then find the entry point that minimizes the sound path to the pixel as:

$$t_{Pi} = 2\left(\frac{\left|\vec{r}_{(1,i)}\right|}{c_1} + \frac{\left|\vec{r}_{(2,i)}\right|}{c_2}\right) \tag{9}$$

where $\vec{r}_{(1,i)}$ is the sound path from the position y_i to the entry point e_i in the first medium with a propagation of sound c_1, and $\vec{r}_{(2,i)}$ is the distance from e_i to the pixel P in the second medium with sound speed c_2. Then, the SAFT process is computed from evaluating (7). It is worth to remark that when operating with a solid wedge the interface geometry does not change, and hence, (9) can be evaluated only once before starting the acquisition, reducing the computing load during the scan.

A. Phase Coherence Imaging (PCI)

The PCI technique evaluates, for each point of the output image, a coherence factor between 0 and 1. A low coherence is representative of signals that do not come from the focus, as occurs with noise, side-lobes, grating lobes and artefacts. Thus, when the beamformer weights its output by the coherence factor these indications are cancelled. On the other hand, the output image keeps those indications that have a coherence factor close to the unit, which are more probably produced by in-focus reflectors.

The coherence factor considers the phases of the aperture data as a distribution in the range (-π, + π] and measures its dispersion (i.e. standard deviation, variance, etc.) [27, 28]. Furthermore, the Sign Coherence Factor (SCF) was proposed for simplifying calculations, using the sign (b_i) of the signals as a single bit discretization of the phase. The SCF factor is calculated for each pixel P as follows:

$$SCF_P = 1 - \sqrt{1 - \left(\frac{1}{M} \sum_{i=1}^{M} b_i(idx_{Pi}) \right)} \tag{10}$$

where $b_i(idx_{Pi})$ is the sign of the signal a_i received by the array at position y_i, in the elevation plane located at x = cte, for the round-trip TOF indicated by the index idx_{Pi}. In other words:

$$b_i = \begin{cases} +1 \xrightarrow{if} a_i(idx_{Pi}) \geq 0 \\ -1 \xrightarrow{if} a_i(idx_{Pi}) < 0 \end{cases} \tag{11}$$

Therefore, the amplitude of each pixel P is computed according to (7) and weighted by its SCF given by (10) to obtain an output pixel according to the PCI technique as follows:

$$I_P{}^{SCF} = \left| SCF_P \cdot I_P \right| \tag{12}$$

Ideally, the acquisitions should be done keeping $dy \leq \lambda/2$ to avoid the grating lobes formation in the output image [25]. Although complying with this requirement, the monostatic SAFT process results in the formation of artefacts in the image, which reduce the contrast [29]. For this reason, the use of SCF is essential for suppressing spurious indications in the output image, as well as improving the resolution and contrast [30, 31]. These features, even allow working with larger separations of dy, reducing the required bandwidth and processing power while maintaining a good contrast.

IV. Experimental Results

The image composition was performed using Python running on an Intel Core i7-3770 8-core @3.4GHz 64-bit with 8GB of RAM, and PyOpenCL [32] was used for parallel computing on the hardware AMD Asus Strix-R9 390X- DC3 of 8GB RAM.

Several scans of different VOIs following the scheme on Figure 7 were performed, mechanically moving the array attached to the mask and acquiring 2D low-resolution images in linear format (B-Scans). The

array position was registered by an optical encoder and as the VOI is scanned the acquired images are stored in memory and then saved to hard disk. Data capture was performed using a PA SITAU-311 system (DASEL, Spain) of 32 channels multiplexed to 128, operating with a 5 MHz linear array of 128 elements and pitch 0.5 mm (Imasonic, France). All experiments were performed with a sampling frequency of 40 MHz and using an active aperture of 32 elements with dynamic focusing in real-time.

The mask proposed for immersion inspections was built using industrial silicone rubber (RTV - Noviplast, Argentina) vulcanized with HS II catalyst. The parts were mixed with a 100:5 ratio of mass respectively, and then a negative mould was filled. The polymer was left around 24 hrs for curing and subsequent demoulding. The wedge construction time can be shortened using higher temperature as well. The small air bubbles formed during the polymer preparation are left, as long as they act as point scatters that increase attenuation inside the mask.

A. Immersion beam profile

The beam profile in the elevation plane produced by the silicone mask was measured by pulse-echo using a spherical reflector (0.8 mm in diameter), located at 50 mm from the array surface immersed in degassed water. The VOI under test has a size of 50x70x35 mm (dimensions of azimuth, elevation, and depth, respectively) which was sampled taking successive 2D low-resolution images separated at dy = 0.1 mm ($\approx\lambda/3$ for a 5 MHz array in water).

Figure 9A shows the C-Scan obtained with the linear array without the mask, and in Figure 9F the PSF (point spread function) in the elevation direction. As the array is not focused in elevation, the width of the PSF at -6 dB is ≈ 10 mm, similar to the array width W. When the mask is used, a loss of lateral resolution in the elevation direction is appreciated in a single image (Figure 9B). The half-angle of divergence measured from the PSF for a 6 dB drop is $\alpha_y \approx 6$ °, similar to the theoretical value, confirming an effective reduction of the aperture size on the elevation direction. Furthermore, no important artefacts are seen, confirming that most of the sound propagated within the mask is not refracted out to the water. The spatial diversity that introduces the broad beam can be observed through an end-view of the VOI along the elevation plane (Figure 9C). This image, also called D-Scan is a representation of the yz plane, obtained by taking the maximum amplitude value of the samples in a cross-direction to the VOI.

After applying the proposed algorithm, thin and high-resolution slices of the VOI are obtained. Figure 9D shows a C-Scan with improved resolution in the elevation direction with regard to the no-mask acquisition. The side-lobes relative amplitude is -20 dB and a considerable improvement in the SNR is observed because of SAFT averaging. From the PSF in Figure 9F, the reflector length for a 6 dB drop is approximately 0.7 mm, value that matches its real dimension. Furthermore, this value can be considered as the width of the slices in the elevation direction, much less than that obtained with the array alone.

The use of the PCI allows improving even more the output image quality, by reducing the lobes artefacts (Figure 9E). After applying the SCF factor, the dynamic range in the images is improved by about 30 dB and a narrower main lobe is obtained (Figure 9F). Finally, the processing of the 250 output images necessary for the VOI reconstruction was performed at rate of 1 ms/image. This computing time includes data loading into GPU memory, composition and storage.

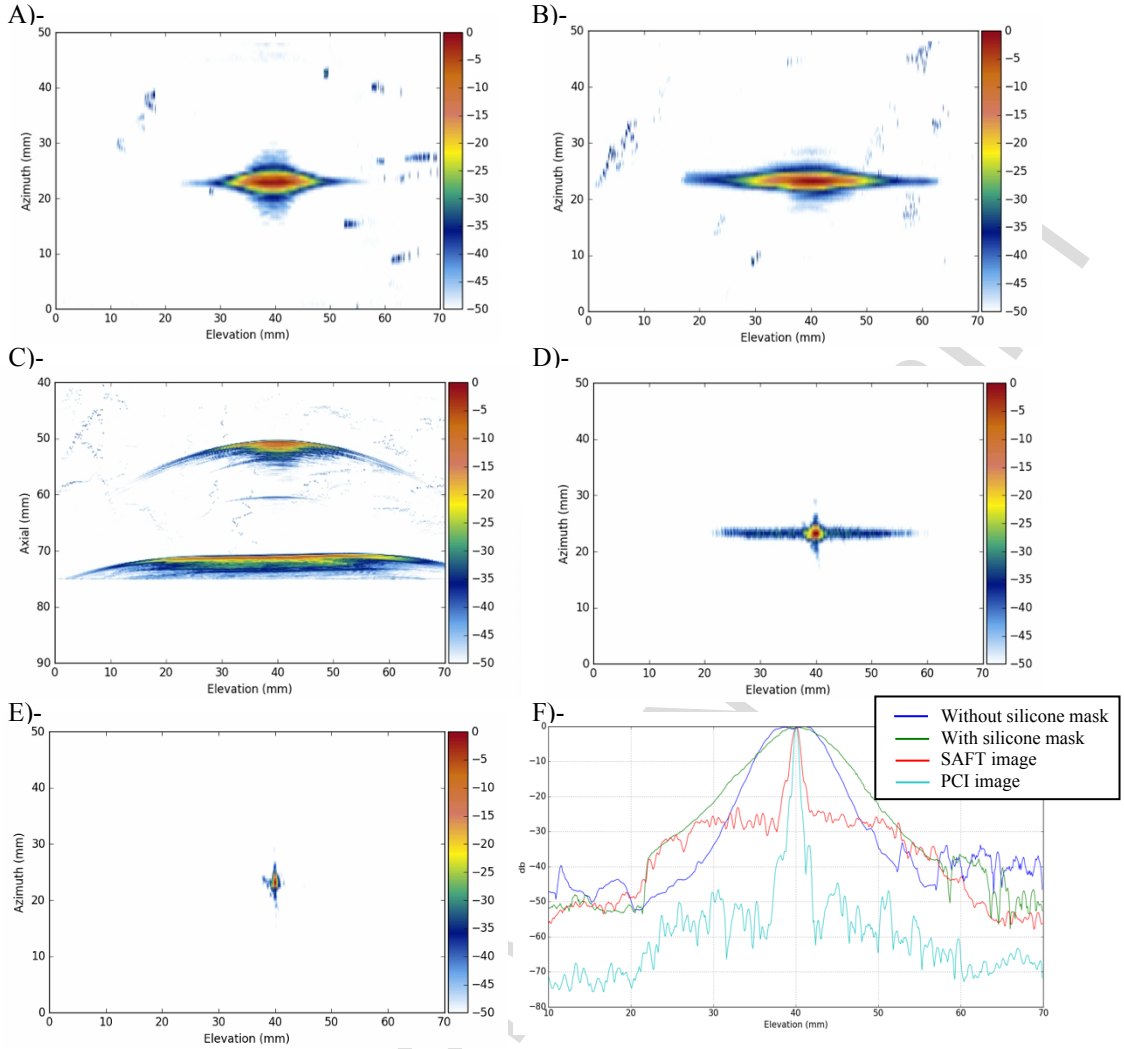

Figure 9. Experimental results of immersion inspection for a single reflector using dy = 0.1 mm as spatial resolution (dynamic range for all images 50 dB). **A) -** C-scan using a conventional linear phased array. **B) -** C-scan using the silicone mask. The reflector size stretches along the elevation direction due to the broading of the emitted beam. **C) –** End view (D-Scan) of the VOI in which can be seen the mask effect. The broad beam produces the scattered information of the reflector making a hyperbola on the image. **D) -** Improved C-scan image by coherent addition of partial images which are selected as a function of the axial according to (4). **E) –** The use of the PCI allows reducing the side lobes observed in D. **F) -** PSF functions measured at 40 mm of depth in degassed water for cases A, B, D and E.

B. Immersion inspection with water-aluminium interface

The silicone mask mounted on the array probe was used for inspecting an aluminium block immersed at a depth of 56 mm in degassed water. The sample has a centred conical-tip bottom hole as a reference reflector (Figure 10A). The scanned VOI has a size of 35x80x40 mm (dimensions of azimuth, elevation, and depth, respectively). The 2D low-resolution images were acquired every 0.5 mm, which means a sampling interval $dy < \lambda/2$ in aluminium.

As in the previous case, the hole-tip appears stretched in elevation in the C-scan image obtained with the silicone mask (Figure 10B). In this case, this effect is more pronounced because of refraction at the water-aluminium interface. The α_y value measured from Figure 10E results in 26.5 ° at -6 dB, which corresponds to an incident beam angle of 6º, in agreement with the theoretical calculations. Before generating the output image according to (7), the focal laws were pre-calculated applying (9) to reduce the computational load during beamforming. Figure 10C shows the C-Scan after processing the set of 2D

low-resolution images, which gives a considerable improvement the elevation resolution and SNR. The side-lobes have been reduced below -20 dB and the reflector width at -6 dB is 1 mm. After applying the PCI processing (Figure 10D), the image dynamic range increases by approximately 12 dB and lateral resolution is also improved (Figure 10E). These high-resolution images are beamformed at a higher rate than the previous case (0.4 ms/image) due to a higher spatial interval between images and fewer A-Scan samples since the sound propagation velocity in aluminium is 4 times greater that in water.

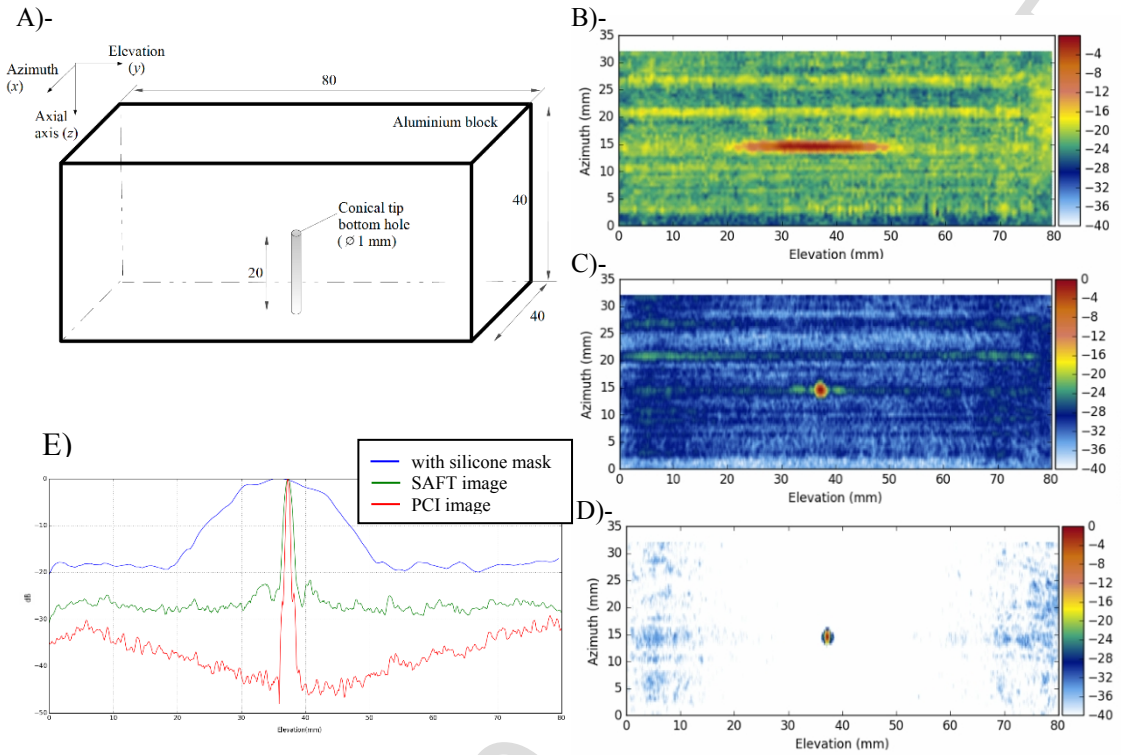

Figure 10. A) - Aluminium test-block used for testing in immersion. The mechanical interval between images was set to 0.5 mm. **B) -** Obtained C-scan using the silicone mask without applying the beamforming processing. **C) -** Processed C-Scan after imaging. **D) -** Improvements in the output image using PCI technique. **E) -** PSF lateral pattern of the tip, located at 20 mm of depth in aluminium. Dimensional units: mm, dynamic range of images 40 dB

C. Mask for contact inspections

The mask designed for contact applications was made of Rexolite® and mounted as a zero-degree wedge. An aluminium test-block was mechanized with different types of reference reflectors for evaluating the proposed method performance (Figure 11). The experiments were divided into three volumes of 55x60x30 mm (dimensions of azimuth, elevation, and axial, respectively) for evaluating the response of each reflectors separately. As a sampling criterion for the three cases, 2D low-resolution images were acquired every 0.3 mm (that is $dy \approx \lambda/3$ for aluminium). Moreover, focusing delays required for generating the focal laws through the flat-interface were previously obtained to reduce the computing load during beamforming. As a result, the algorithm of composition achieves a frame rate of 0.4 ms/image.

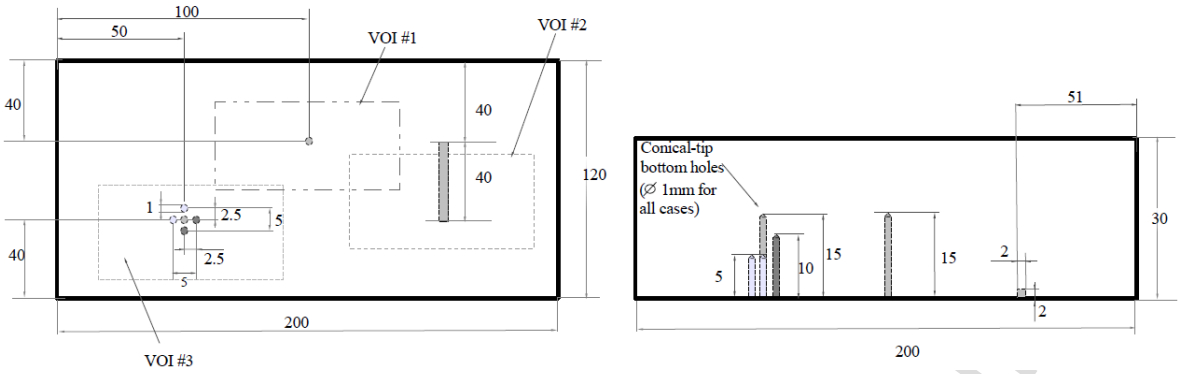

Figure 11. Aluminium test-block used for contact testing. **A) -** Top view. **B) -** Side view.

C.1 VOI #1: bottom hole

This test was performed to determine the elevation beam profile at the conical-tip of a bottom hole of 1 mm diameter and 15 mm height. As in the previous cases, the reference reflector is observed with an elongated shape in the elevation direction in the low-resolution C-Scan image. The SNR deterioration is noticeable due to the higher attenuation of Rexolite with regard to water (Figure 12A). The elevation beam profile in this case has 40º of divergence, which can be determined from the PSF lateral profile at 6 dB drop (Figure 12D). In addition, the measured response of the reflector using the mask is very close to the simulated one (blue trace in Figure 12D). This shows that the proposed design behaves according to the theoretical expectations, that is, the half-angle of divergence is ≈ 14º in the elevation direction inside the mask. After processing the input images with the proposed algorithm, the C-Scan view of the VOI presents a significant improvement in the SNR, as well as in the elevation resolution and the reflector can be correctly detected in the elevation direction (Figure 12B). From the 6 dB drop in the PSF criterion, it is 1 mm long. Finally, a larger dynamic range (≈ 25 dB) and improved lateral resolution are achieved with the PCI technique (Figure 12 C).

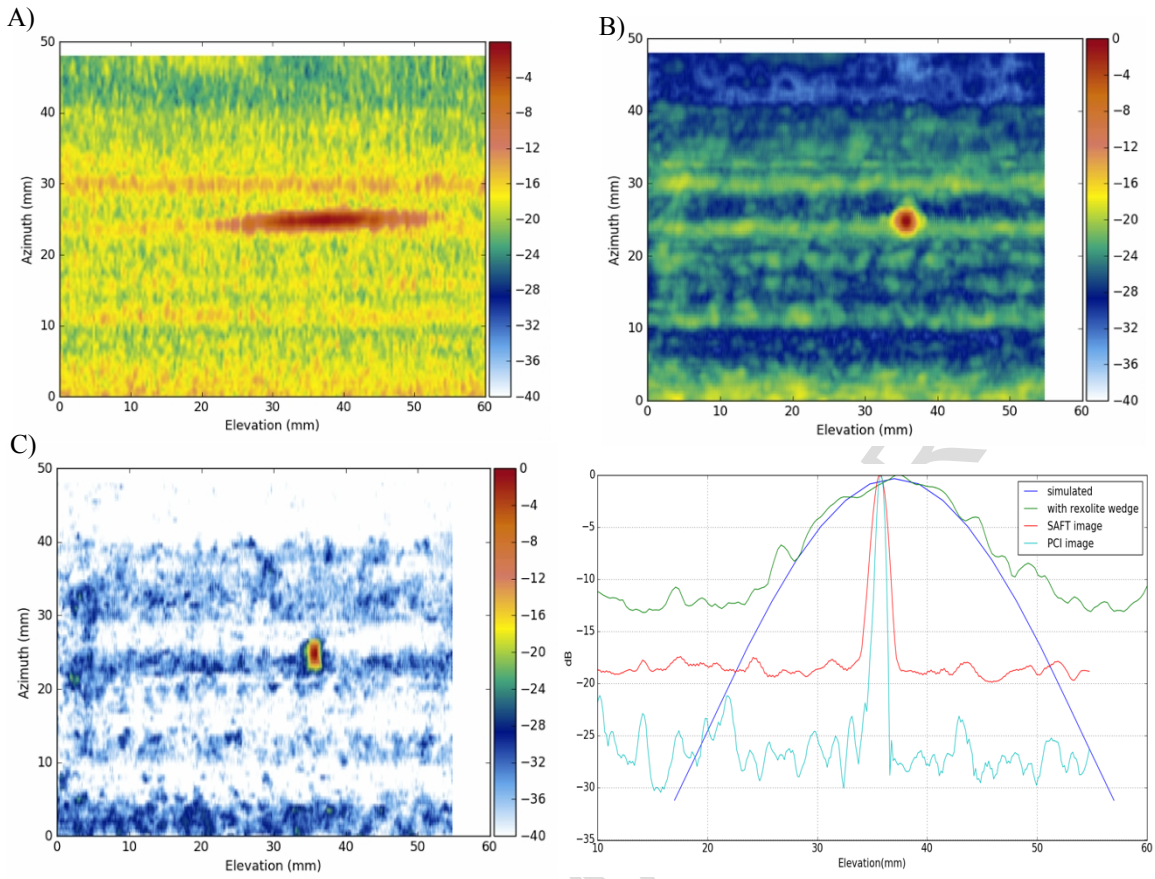

Figure 12. Contact inspection results for the VOI# 1. A)- C-Scan using the trapezoidal wedge. B)- C-Scan image achieved after imaging. C)- Output image applying PCI. D)- Comparison of PSF obtained for the three cases. Images represented with a dynamic range of 40 dB.

C.2 VOI#2: notch

In this case, the scanned VOI contains a rectangular notch of 2x2 mm square cross-section and 40 mm length. Since the reflector is not high enough, the original C-Scan gate includes the notch reflection as well as the echoes originated at the bottom of the piece (Figure 13A). A slight improvement in SNR is obtained after imaging following the proposed process. However, the notch reflection is 15 dB above of the backwall echo (Figure 13B). Additionally, using the PCI technique, the notch can be observed much more defined and can be correctly quantified in both the elevation and the azimuth directions. Moreover, the backwall echoes become reduced (Figure 13C).

In the reconstructed VOI, the notch presents a small inclination which was originated by a misalignment between the mechanical scan and the notch orientation. This is not observed in the unprocessed image because the lack of enough resolution in the elevation direction.

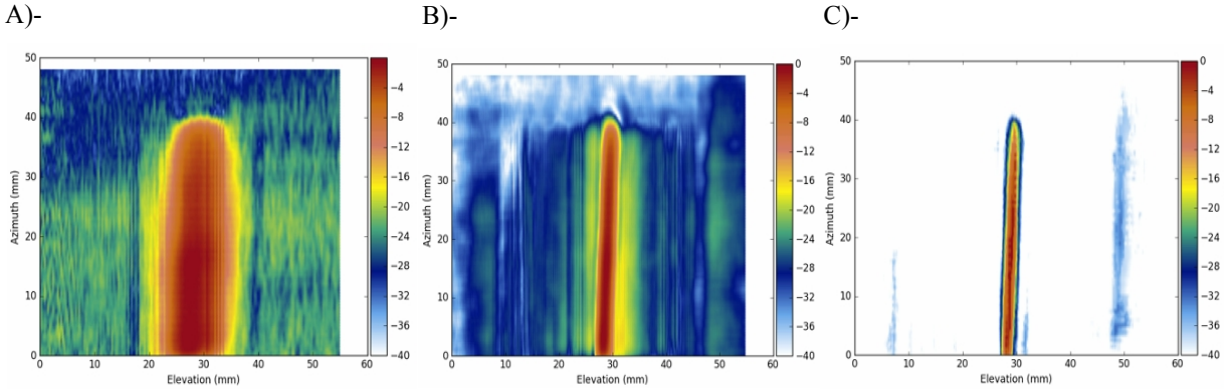

Figure 13. C-Scan views for the rectangular notch of VOI#2. **A)-** Acquired information using the trapezoidal wedge. **B)-** C-Scan after imaging. **C)-** C-Scan image using the PCI technique. The images have been represented with a dynamic range of 40dB.

C.3 VOI#3: set of holes

In this case, the VOI has a set of 5 closely spaced conical-tip bottom holes at different depths. In this case, the holes along the elevation direction are located closer than the resolution that can be achieved using a conventional linear array (Figure 11). After performing the inspection with the mask, the broad beam makes not possible resolving the reflectors in the elevation direction in the C-Scan image (Figure 14A), while it is possible to barely distinguish two indications along the azimuth direction.

After applying the proposed algorithm, the new C-Scan presents a higher resolution in the elevation direction (Figure 14B). Furthermore, on the D-Scan view the different heights of the holes can be easily determined (Figure 14C). Finally, an important improvement in the SNR is achieved using the PCI (Figure 14D), which reduces artefacts and side-lobes.

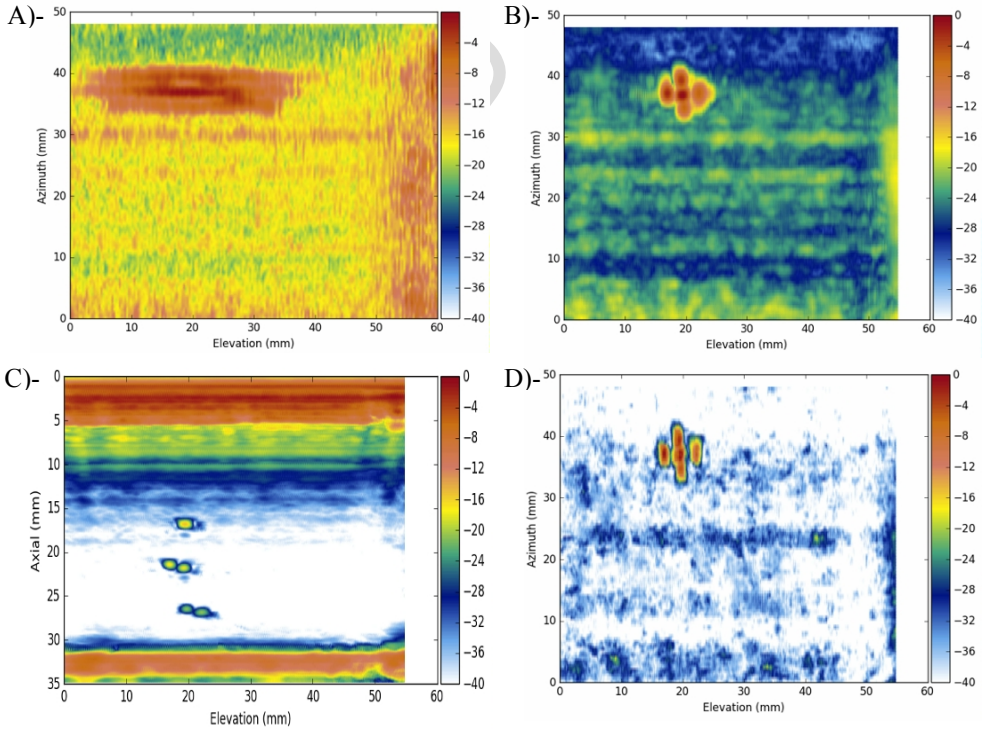

Figure 14. Results for VOI#3. **A) -** C-Scan acquired with the trapezoidal mask. **B) -** C-Scan after imaging**. C) -** D-Scan image of the VOI. **D) -** C-Scan using the PCI technique. Dynamic range of all images 40 dB.

D. Inspection of a nuclear coupon

A reference block used in the nuclear industry was inspected with the proposed technique. The sample consists of two 304 stainless steel plates joined by a butt weld with a symmetrical J-type bevel, and the reinforcement removed (Figure 15). The assembly has on the top a flat surface and on the bottom a welded cladding layer of variable thickness between 4.5 and 8 mm. The minimum block thickness is 52 mm and its maximum is 60 mm, just below the root weld reinforcement. Four side non-pass through holes of 2 mm diameter and 25 mm length each one, were machined as reference reflectors. One of the holes was located at the base-material-cladding interface. The others were positioned around the weld: one near the weld toe, other between root and cladding and the last one between the weld bevel and the cladding interface.

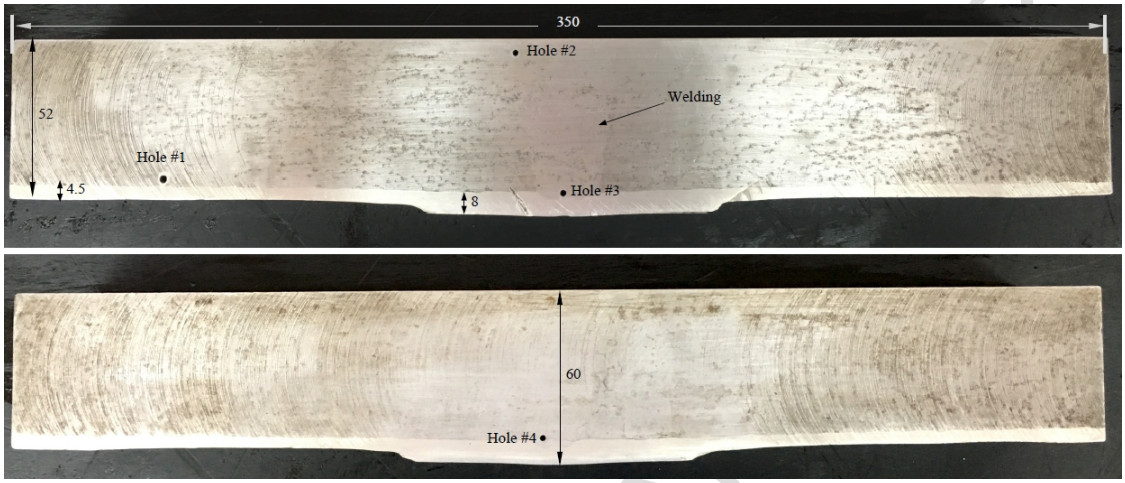

Figure 15. Side-views of the test-block made from materials for nuclear applications.

The test-block was inspected by immersion in degassed water. The silicone mask was used leaving a water path of 43 mm. The piece was spatially sampled by acquiring 2D low-resolution images in the elevation direction every 0.35 mm ($dy \approx \lambda/3$ for steel), covering a total length of 350 mm. The focal laws were previously calculated, as the interface shape and relative position is constant along the scan.

Figure 16 shows the resultant image after applying the proposed beamforming algorithm. The step just below the weld root can be observed in the D-Scan image, holes # 3 and # 4 can be clearly identified (Figure 16A). However, reflector # 2, which is close to the surface, cannot be observed easily. In this case, the use of the PCI technique allows improving contrast by highlighting this reflector (Figure 16B). In fact, the dynamic range of the image with PCI improves significantly with respect to the initial one. This comparison is evident when representing both VOIs with a full scale of 70 dB. Moreover, in the D-Scan image after applying the PCI technique it is also easier to distinguish the backwall echo from the cladding interface.

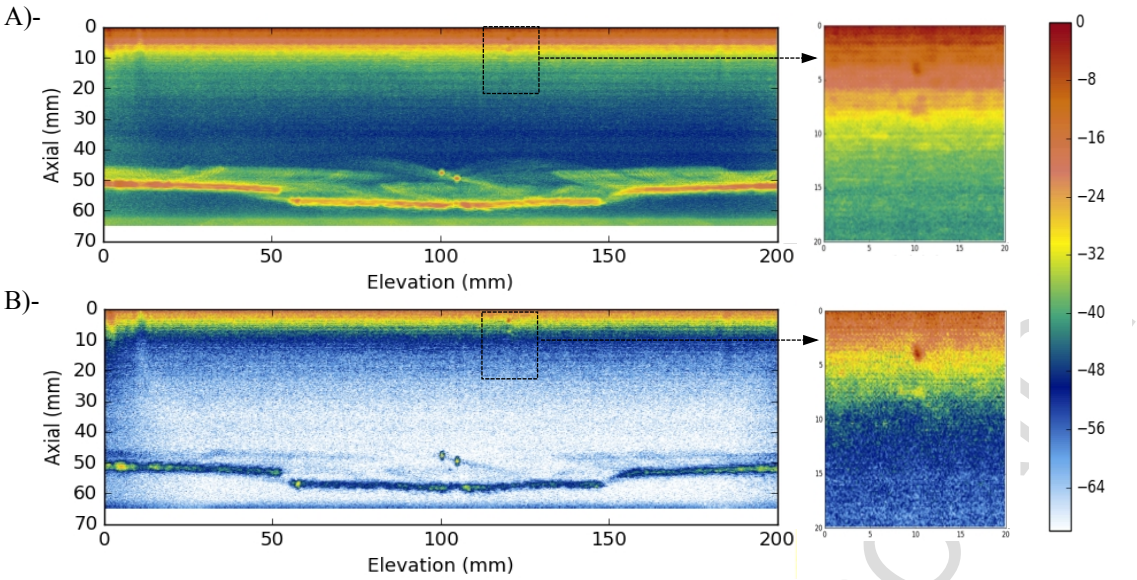

Figure 16. A) - Test-block D-Scan image after imaging (welding zone). **B) -** D-Scan image using PCI. Dynamic range of images 70dB. In both cases, a zoom area around the echo from reflector #2 is given to compare how the indication is highlighted using PCI.

Finally, it is possible to locate and evaluate the extent of all side holes using the C-Scan images. This is achieved by adjusting the gate range to display the reconstructed VOI at different depths. For instance, a C-Scan image can be obtained by setting the gate range in 0 to 10 mm of the sample. In this case, the hole #2 can be barely distinguished (Figure 17A). After adjusting the visualization gate range in 45 to 52 mm, a new C-Scan image is achieved where holes #1, #3 and #4 are clearly seen (Figure 18A). In both cases, the quality of the obtained C-Scan images is further improved using the PCI technique (Figure 17B and 18B), particularly the detection of hole #2, which is near to the surface, and hole #1, which is masked by the background artefact that surrounds it.

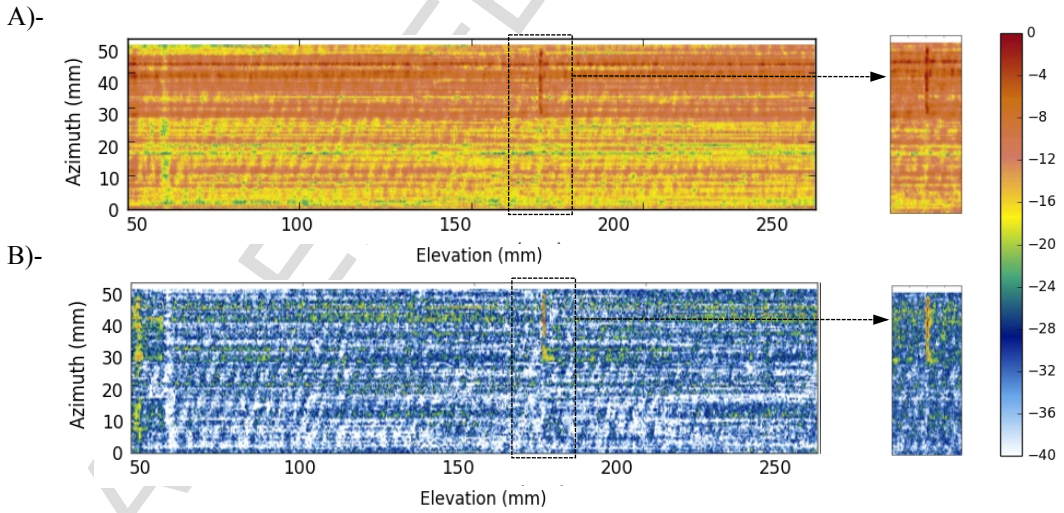

Figure 17. A) - Test-block C-Scan image after imaging adjusting a gate range in 0 -10 mm. **B) -** C-Scan image using PCI. Dynamic range of images 40dB. Only the hole #2, which is close to the surface is viewed. In both cases, a zoom area around the echo from reflector #2 is given to compare how the indication is highlighted using PCI.

A)-

B)-

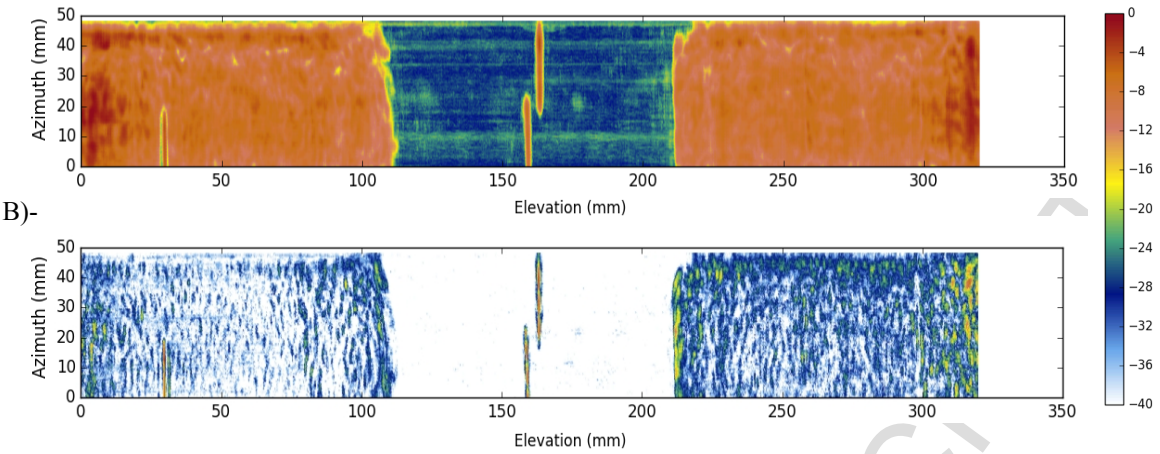

Figure 18. A) - Test-block C-Scan image after imaging (welding zone). **B) -** C-Scan image using PCI. Dynamic range of images 40dB. Holes #1, #3 and #4 are viewed adjusting the C-Scan visualization gate range in 45 – 52 mm.

Table 1 summarizes the computing times to reconstruct the different VOIs analyzed above. The expressed time is the required to produce the output VOI indicated in voxels, and includes the time of data loading in the GPU memory, composition and data storage on disk.

Sample test	Condition	Input VOI (*z,x,y*) [samples]	Output VOI (*z,x,y*) [voxels]	VOI sampling resolution [mm]	Processing time [sec]
Single reflector	Immersion	2968, 97, 451	150, 97, 249	0.1	0.27
Test-block of nuclear use	Immersion	814, 97, 642	260, 97, 1280	0.3	1
Aluminium test-block	Contact	506, 97, 201	233, 97, 366	0.25	0.15

Table 1. Summary of the computing time required for processing the different sizes of VOIs.

Finally, the Mayavi [31] application was used for 3D representation (Figure 19). The processed data cube is positioned in a 3D space, in which each pixel constitutes a voxel. In the application is possible to assign the different opacity values to each voxel and to show the inside of the block by selecting layers. It is also possible to make cuts, rotate the image, adjust brightness, views, etc. in consequence, this method of representation can provide a fast and easier evaluation of inspection results (Figure 19).

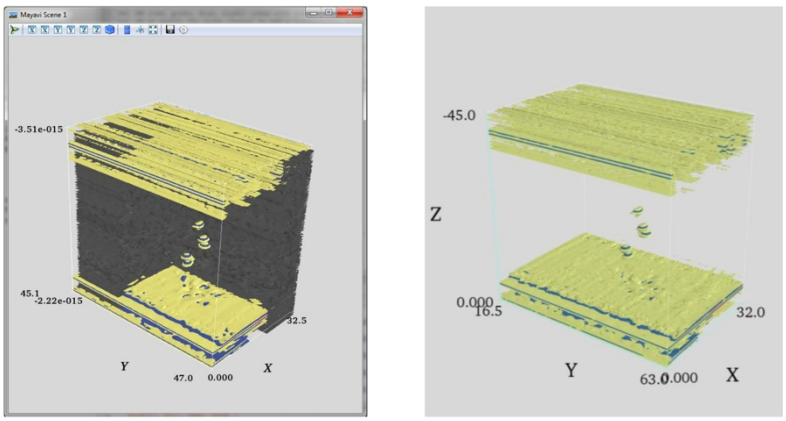

Figure 19. 3D representation of the VOI#3 which contains 5 bottom holes (Figure 11) is shown in the Mayavi environment (left). The interior can be evaluated by adjusting the voxels opacity (right).

V. Conclusions

An image method which improves the elevation resolution of a conventional linear array was presented, based on combining three ultrasonic imaging techniques: PA, SAFT and PCI. Moreover, the developed strategy is suitable for NDT in industrial applications, which allows performing a 3D ultrasonic imaging of the volume under test by using the 2D images acquired with a conventional phased array system.

The proposal is highly effective and efficient, since the costs and complexity of the equipment are considerably reduced with regard to matrix arrays. In addition to a conventional phased-array system and transducer, only a mask/ for decreasing the active area of the array elements in the elevation direction and a standard low-cost parallel processing platform are required.

For immersion inspections, a silicone mask is proposed, which can be easily be reproduced and modified to change the beam divergence in the elevation direction according to the material properties under test. For direct contact inspections, a trapezoidal-shape mask was designed. In this case, the height must be selected as a function of the sample thickness to be tested.

Although the use of the mask reduces the SNR of each acquired image, the averaging effect of the SAFT partially recovers it, giving acceptable noise levels, while the coherent composition improves resolution and defects detectability and sizing. The use of the PCI technique further reduces side lobes, grating lobes and artefacts and improves simultaneously the lateral resolution of the output image.

It is worth to note that the proposed method allows a fast-mechanical scanning. While the 2D low-resolution images generated by the phased-array equipment are buffered in real-time, the output images can be processed concurrently in an external computer to build the high-resolution 3D-image. The imaging SAFT reconstruction can be performed on a GPU platform at high speed because data volume is kept low by using the phased-array technique in the azimuth plane.

This new and simple imaging procedure could be easily implemented in several current applications, where the component surface is flat, or it is well known. Future work includes extending this concept for the case of complex shape surfaces, even in the case when they are not precisely known (i.e. autofocusing required).

Acknowledgments

This work was partially founded by the projects: iCoop-20116 of the Spanish National Research Council, DPI2013-42236-R of the program “Research challenges” of the Spanish Ministry of Economy and Competitiveness and PICT-2014-1768 of the ANPCyT (Argentina).

References

[1]. T. Armitt. “Phased arrays not the answer to every application”, 9th European NDT Conference – ECNDT Proceedings, (2006) Berlin, Germany.
[2]. A. Fenster, D. B. Downey, H. N. Cardinal. “Three-dimensional ultrasound imaging”, Phys. Med. Biol. Vol 46, pp. R67–R99 (2001).
[3]. R. Ohbuchi, D. Chen and H. Fuchs. “Incremental volume reconstruction and rendering for 3D ultrasound imaging”, Proc. of SPIE - The International Society for Optical Engineering, pp. 312-323 (1992).
[4]. J. Carr. “Surface reconstruction in 3D medical imaging”. PhD thesis, Univ. of Canterbury, New Zealand (1996).
[5]. P. H. Mills, H. Fuchs. “3D ultrasound display using optical tracking”, Proc. of the First Conf. on Visualization in Biomed. Comp., pp. 490 –497 (1990).
[6]. T. R. Nelson and D. H. Pretorius. “Three-dimensional ultrasound imaging”, Ultrasound in Med. & Biol., Vol. 24 (9), pp. 1243–1270 (1998).
[7]. P. Hoskins, K. Martin, and A. Thrush, eds. “Diagnostic Ultrasound: Physics and Equipment”, Cambridge University Press. New York, USA (2010).
[8]. D. Wildes, R. Chiao, C. Daft, et al. “Elevation performance of 1.25D and 1.5D transducer arrays”, IEEE Trans. UFFC. Vol 44 (5), pp. 1027 – 1037 (1997).
[9]. P.-C. Li and J.-J. Huang, “Efficient Dynamic Focus Control for Three-Dimensional Imaging Using Two-Dimensional Arrays”, IEEE Trans. UFFC. Vol. 49 (9), pp. 1191-1202 (2002).
[10]. R. Chiao, K. Rigby, and D. Wildes, “Optimization of 1.5D arrays”, IEEE Ultrasonics Symp., pp 1835-1838 (1998).
[11]. S. W. Smith, O. T. von Ramm, and H. G. Pavy. “High-speed ultrasound volumetric imaging system - Part I: Transducer design and beam steering,” IEEE Trans. On UFFC. Vol. 38, pp. 100-108 (1991).
[12]. E. Light, R. Davidsen, et al. “Progress in two-dimensional arrays for real-time volumetric imaging”. Ultrason Imaging. Vol 20(1), pp. 1-15 (1998).
[13]. G. R. Lockwood, J. R. Talman, and S. S. Brunke, “Real-Time 3-D Ultrasound Imaging Using Sparse Synthetic Aperture Beamforming”. IEEE Trans. On UFFC. Vol. 45 (4), pp. 980-988 (1998).

[14]. Z. M. Benenson, A. B. Elizarov, T. V. Yakovleva and W. D. O'Brien, "High-resolution and fast 3D ultrasonic imaging technique". IEEE Ultrasonics Symposium (IUS 2003). Vol. 2, pp. 1561-1564 (2003).

[15]. V. Cong, and H. Q. Linh, "3D medical image reconstruction". Biomedical Engineering Department (2002).

[16]. Y. Dai, J. Tian, D. Dong, G. Yan, and H. Zheng, "Real-time visualized freehand 3D ultrasound reconstruction based on GPU". IEEE Trans. on Information Technology in Biomedicine. Vol. 14(6), pp. 1338 -1345 (2010).

[17]. S. Kitazawa, N. Kono, al., "A three-dimensional phased array ultrasonic testing technique". 7th Int. Conf. on NDE in Relation to Structural Integrity for Nuclear and Pressurized Components. Yokohama, Japan (2009).

[18]. H. Karasawa, T. Ikeda1, S. Matsumoto, T. Hamajima, and H. Isobe, "3D-SAFT ultrasonic inspection equipment – Matrixeye™" 7th Int. Conf. on NDE in Relation to Structural Integrity for Nuclear and Pressurized Components. Yokohama, Japan (2009).

[19]. Jr. Schmerr, W. Lester, "Fundamentals of ultrasonics phased arrays", Springer, New York (2015).

[20]. K. Zell, J. Sperl, et al., "Acoustical properties of selected tissue phantom materials for ultrasound imaging", Physics in medicine and biology, vol. 52 (20), pp. 475-484 (2007).

[21]. P. Calmon, S. Mahaut, S. Chatillon, R. Raillon, "CIVA: an expertise platform for simulation and processing NDT data", Ultrasonics, 44, pp. 975-979 (2006).

[22]. C. H. Frazier and W. D. O'Brien, "Synthetic aperture techniques with a virtual source element". IEEE Trans. UFFC. Vol. 45 (1), pp. 196–207 (1998).

[23]. J. T. Ylitalo and H. Ermert, "Ultrasound synthetic aperture imaging: monostatic approach". IEEE Trans. UFFC. Vol. 41 (3), pp. 333-339 (1994).

[24]. M. Karaman, P.C. Li, M. O'Donnell, "Synthetic Aperture Imaging for Small Scale Systems". IEEE Trans.on UFFC, Vol. 42 (3), pp. 429- 442 (1995).

[25]. M. Karaman and M. O'Donnell, "Subaperture processing for ultrasonic imaging". IEEE Trans. UFFC. Vol. 45 (1), pp. 126-135 (1998).

[26]. J. Krautkrämer, H, Krautkrämer, "Ultrasonic Testing of Materials", Springer -Verlag (1990).

[27]. C. Fritsch, M. Parrilla, J. Camacho, "Method and apparatus for correcting ultrasound images by means of phase analysis", Pat. WO/2010/018282, 18 Feb. 2010.

[28]. J. Camacho, M. Parrilla, C. Fritsch, "Phase Coherence Imaging", IEEE Trans. UFFC, Vol. 56 (5), pp. 958-974 (2009).

[29]. C. J. Martín, O. Martínez, L. G. Ullate, A. Octavio, G. Godoy, "Reduction of Grating Lobes in SAFT Images", Proc. IEEE IUS, pp. 721-724 (2008).

[30]. J. Camacho, J. Brizuela, C. Fritsch, "Grain-noise reduction by phase coherence imaging", AIP Conference Proceedings, Vol. 29, pp. 855-862 (2010).

[31]. J. Camacho, M. Parrilla, C. Fritsch, "Grating-lobes reduction by application of Phased Coherence Factors", Proc. IEEE IUS, Rome, Italy, pp. 341-344, (2009).

[32]. A. Klöckner, N. Pinto, Y. Lee, B. Catanzaro, P. Ivanov, A. Fasih, "PyCUDA and PyOpenCL: A scripting-based approach to GPU run-time code generation", Parallel Computing, Vol. 38 (3), pp. 157-174 (2012).

[33]. P. Ramachandran and G. Varoquaux, "Mayavi: 3D Visualization of Scientific Data", IEEE Comp. in Science & Eng. Vol 13 (2), pp. 40-51 (2011).